**Key Points:**
- Dense array monitoring shows delay times (hours-to-days) and offset activation distances (up to a km) from injection time
- There are highly permeable fracture networks within the reservoir, based on b-values, event timing, MTI and anisotropy analysis
- Pore pressure perturbation along existing fracture networks resulted in fault activation at a distance

# Large-Scale Fracture Systems Are Permeable Pathways for Fault Activation During Hydraulic Fracturing

**Nadine Igonin[1]** , **James P. Verdon[2]**, **J.-Michael Kendall[3]**, and **David W. Eaton[1]**

[1]Department of Geoscience, University of Calgary, Calgary, Alberta, Canada, [2]School of Earth Sciences, University of Bristol, Wills Memorial Building, Bristol, UK, [3]Department of Earth Sciences, University of Oxford, South Parks Road, Oxford, UK

**Abstract** Induced seismicity due to fluid injection, including hydraulic fracturing, is an increasingly common phenomenon worldwide; yet, the mechanisms by which hydraulic fracturing causes fault activation remain unclear. Here we show that preexisting fracture networks are instrumental in transferring fluid pressures to larger faults on which dynamic rupture occurs. Studies of hydraulic fracturing-induced seismicity in North America have often used observations from regional seismograph networks at distances of 10s of km, and as such lack the resolution to answer some of the key questions about triggering mechanisms. To carry out a more detailed analysis of the mechanisms of fault activation, we use data from a dense sensor array located at a hydraulic-fracturing site in Alberta, Canada. The spatiotemporal distribution of event hypocenters, coupled with measurements of seismic anisotropy, reveal the presence of preexisting fracture corridors that allowed communication of fluid-pressure perturbations to larger faults, over distances of 1 km or more. The presence of preexisting permeable fracture networks can significantly increase the volume of rock affected by the pore-pressure increase, thereby increasing the probability of induced seismicity. This study demonstrates the importance of understanding the connectivity of preexisting natural fractures for assessing potential seismic hazards associated with hydraulic fracturing of shale formations and offers a detailed case exposition of induced seismicity due to hydraulic fracturing.

**Plain Language Summary** Felt earthquakes have been observed in North America, Asia and the U.K. during, or shortly after, hydraulic fracturing for shale gas development. An increase in fluid-pressure is widely regarded as the primary mechanism for fault activation, but current models do not adequately explain time delays (hours-to-days) and activation distance (up to 1 km) from the injection well. Using high-resolution data acquired in close proximity to hydraulic-fracturing operations, we show that preexisting natural fracture systems can provide permeable conduits for diffusion of fluid pressure to a fault that is of sufficient size to host a felt earthquake. Our model explains both the observed time delay and activation distance and demonstrates that the mapping of fracture networks is an important consideration in risk analysis for induced seismicity.

## 1. Introduction

The association of induced seismicity with hydraulic-fracturing (HF) operations for shale gas extraction is well-established (e.g., Atkinson et al., 2016; Bao & Eaton, 2016; Clarke et al., 2019; Verdon & Bommer, 2020; Zoback & Kohli, 2019). The potential socio-economic impact of hydraulic fracturing-induced seismicity worldwide can be high (Atkinson et al., 2020), as exemplified by a $M_L$ 5.7 event in China in 2018, which resulted in injuries and millions of dollars in damages (Lei et al., 2019). Kao et al. (2018) identified at least five instances in western Canada of $M > 4.0$ induced events, while other notable cases of hydraulic fracturing-induced seismicity have been documented in Ohio (Friberg et al., 2014; Skoumal et al., 2015), Oklahoma (Holland, 2013), and the UK (Clarke et al., 2019; Kettley et al., 2020a). For many published case studies of hydraulic fracturing-induced seismicity, events were recorded using regional seismograph networks at distances of 10s of km (or more), or local monitoring was installed after-the-fact once seismicity had started (e.g., Clarke et al., 2014; Darold et al., 2014; Friberg et al., 2014; Schultz et al., 2015a, 2015b; Skoumal et al., 2015; Wang et al., 2016). With such limitations, further investigation into the causative mechanisms of induced seismicity is often hindered, meaning that competing hypotheses cannot always be conclusively tested (e.g., Deng, Liu, & Harrington, 2016; Schultz et al., 2017).
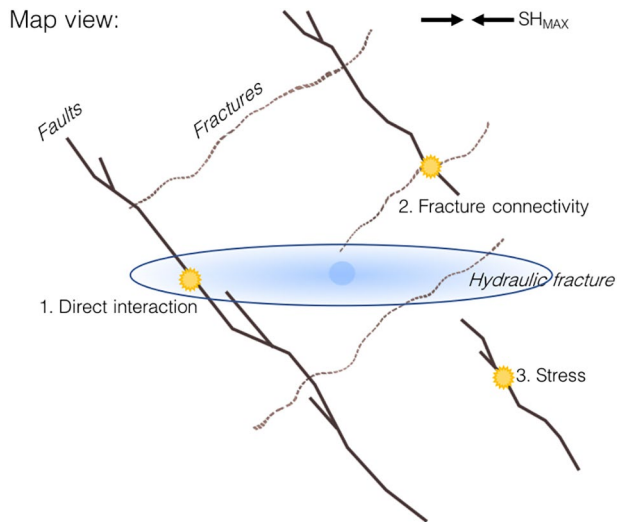
**Figure 1.** Various mechanisms by which hydraulic fracturing may cause fault reactivation: (1) hydraulic fractures (shaded blue region) may directly intersect a fault, (2) preexisting permeable fracture corridors may transmit elevated pore pressures to a fault, and (3) stress transfer through the rock frame may increase the CFS acting on a fault.

Debate persists about the relative contributions of pore-pressure increase or stress transfer in generating induced seismicity, including trade-offs that likely exist between these different mechanisms. For example, questions persist regarding the range of influence of pore-pressure changes or stress perturbations (Goebel et al., 2017; Segall & Lu, 2015), as well as the magnitude of perturbation necessary to trigger induced seismicity (e.g., Hosseini & Eaton, 2018; Westwood et al., 2017; Wilson et al., 2018). Achieving a better understanding of causative mechanisms will have significant implications for strategies used to mitigate induced seismicity. Where regulations pertaining to induced seismicity have been implemented, they are typically tailored toward reacting to cases of induced seismicity rather than prevention or mitigation (e.g., Kendall et al., 2019; Shipman et al., 2018); an improved understanding could aid in preinjection characterization of site-specific seismic hazards, resulting in better options for risk mitigation.

In this study we use data from the Tony Creek dual Microseismic Experiment (ToC2ME), an academic field experiment in Alberta, Canada wherein hydraulic fracturing-induced seismicity was monitored using a purpose-built seismic network (Eaton et al., 2018). The largest events reached a magnitude of $M_W$ 3.2, and over 25,000 events were detected. Using this high-quality dataset, we undertook a detailed investigation of causative mechanisms for fault activation during hydraulic fracturing.

Fault reactivation by subsurface human activities is usually characterized in terms of Mohr-Coulomb effects. The in situ stress field acting on a fault can be resolved into normal ($\sigma_n$) and shear ($\tau$) stresses. Fault slip is expected if the effective shear stress exceeds the Coulomb criterion, given by

$$\tau > \mu(\sigma_n - P) + C, \tag{1}$$

where $P$ is the pore pressure, $\mu$ is the friction coefficient and $C$ is the cohesion. This relationship is often formulated in terms of Coulomb Failure Stress (*CFS*)

$$CFS = \tau - \mu(\sigma_n - P), \tag{2}$$

where a positive change in *CFS* implies that the stress conditions are perturbed toward failure, and a negative change implies that the stress conditions are moving toward greater stability. The Mohr-Coulomb threshold may be reached in one of three ways (or a combination thereof): (1) an increase in the shear stress; (2) a decrease in the normal stress; (3) an increase in the pore pressure.

Figure 1 depicts some of the mechanisms by which fault reactivation may occur during hydraulic fracturing. An increase in pore pressure is a widely recognized causative mechanism for fault reactivation, since hydraulic fracturing, by definition, entails the injection of pressurized fluids into the subsurface. However, shale rocks have exceptionally low permeability, meaning that fluid leakoff and/or diffusion will occur at exceedingly slow rates compared with large-volume injection into a permeable formation (e.g., Atkinson et al., 2016). As such, for most hydraulic-fracturing cases, pore pressures sufficient to activate faults and fractures are expected to be confined to a region no larger than a few hundred meters from the injection point (e.g., Shapiro & Dinske, 2009).

Observations of fault reactivation occurring at larger distances has led some authors to invoke stress transfer via poroelastic coupling as an alternative mechanism for fault reactivation (e.g., Deng et al., 2016; Goebel et al., 2017; Westwood et al., 2017). The stress change from pore-pressure changes, or the deformation associated with tensile fracture opening and shear-slip on preexisting fractures, will affect the stress field in the surrounding rocks, potentially increasing CFS. If the host medium has low permeability, then stress transfer through the rock frame might be expected to act over larger distances than the pore-pressure pulse associated

with injection (e.g., Deng et al., 2016). At the Preston New Road site in the UK, Kettlety et al. (2020b) have demonstrated a strong correlation between the locations of induced events and areas that receive positive CFS changes produced by the tensile opening of hydraulic fractures. Alternatively, Eyre et al. (2019a) show that aseismic (slow) slip along faults can also trigger events at larger distances from a well.

However, the occurrence of seismicity at larger distances from a well does not preclude pore-pressure increase as a causative mechanism, since preexisting fracture corridors within the shale may create more permeable pathways, extending the region of influence of elevated pore pressures along these structures. This mechanism has been proposed for several HF-induced case studies (e.g., Holland, 2013; Schultz et al., 2015a; Westaway, 2017). Zoback & Kohli (2019) also discuss in detail the role of preexisting fracture networks for fault activation during hydraulic fracturing.

In the following sections we introduce the ToC2ME dataset and examine the processes that occurred as faults were activated via the timings, locations, and focal mechanisms of the observed seismicity. After discussing the stress field and interpreting trends identified with measurements of shear wave splitting, we combine these observations with fluid flow and geomechanical modeling, in order to understand which of the above mechanisms are the most likely cause of the fault reactivation.

## 2. Data and Methods

The Tony Creek dual Microseismic Experiment (ToC2ME) is a research-focused field dataset acquired by the University of Calgary, using a suite of geophysical sensors to monitor hydraulic fracturing for shale gas in the Fox Creek area, northwest of Edmonton (Eaton et al., 2018). The monitoring array consisted of 68 shallow borehole stations, with each station comprised of vertical-component 10 Hz geophones cemented at depths of 12, 17, and 22 m and a three-component 10 Hz geophone at 27 m. Additionally, six colocated broadband seismometers and 1 accelerometer were installed at the surface. The average station separation is 500 m, with full azimuthal coverage in the region of the wells. Further details about the ToC2ME dataset can be found in a series of publications (Eaton et al., 2018; Igonin et al., 2018; Poulin et al., 2019; Rodriquez & Eaton, 2020; Zhang et al., 2019).

The site consisted of four horizontal wells drilled into the late Devonian Duvernay Formation at a total vertical depth of approximately 3,400 m. The Duvernay Formation is comprised of fine-grained organic-rich mudstone interfingered with carbonate (Knapp et al., 2017). It is overlain by the Ireton Formation, which consists of a ~300 m thick package of shale with low organic content, and it is underlain by the Beaverhill Lake Group, which consists of variably dolomitized carbonate platform and reef deposits (Knapp et al., 2017). The crystalline Precambrian basement is found at a depth below surface of approximately 4,000 m.

The Fox Creek area in which the ToC2ME site is found has experienced several $M_W \geq 4$ earthquakes that have been attributed to hydraulic fracturing (e.g., Eyre et al., 2019b; Schultz et al., 2017). Dozens of hydraulic-fracturing pads have been linked to earthquakes between $M_W$ 1 and 4 between 2013 and 2019 recorded by regional broadband seismometer networks (Schultz et al., 2020). The induced seismicity in this region is thought to be driven by the presence of regional-scale N/S trending basement-rooted faults that extend into the Palaeozoic sedimentary section (e.g., Eaton et al., 2018; Ekpo, 2020; Eyre et al., 2019b). Although there is limited known natural seismicity in this region, it has been suggested that natural earthquakes can be distinguished from induced earthquakes based on focal depth, since natural earthquakes in this region tend to occur between 5 and 20 km depth, while induced seismicity generally occurs in the upper 4 km (Zhang et al., 2016).

The wells in this dataset were stimulated over a 4-week period in October-November 2016. Well C (see Figure 2) was stimulated first, from north to south along the well, after which the remaining wells were stimulated concurrently in a zipper-like manner. In this study, we focus on the events that occurred during stimulation of Well C. We do this because investigating and understanding the causes of fault reactivation is simpler early in the operation, during the initial stages of fault activation. After faults have initially been reactivated, causative processes become more ambiguous, since it may not be possible to distinguish processes
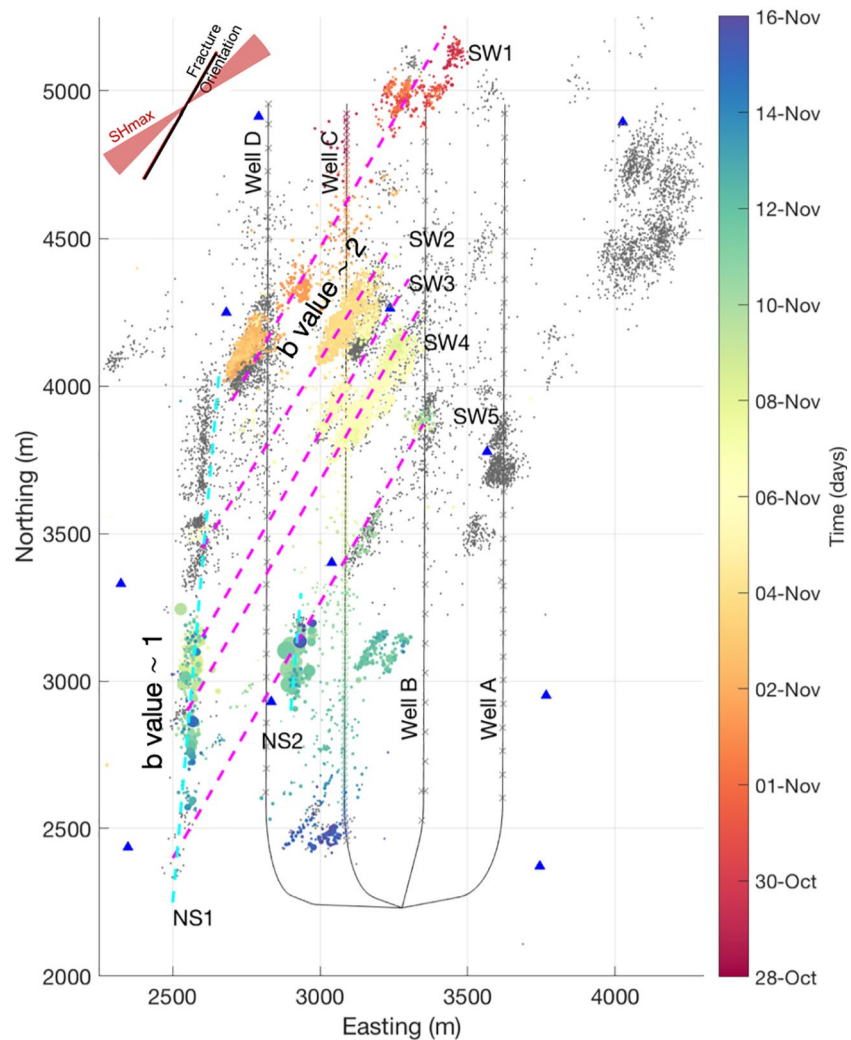
**Figure 2.** Map of events recorded during hydraulic stimulation of Well C (dots colored by occurrence time) and during stimulation of Wells A, B, and D (gray dots) at the ToC2ME site. Blue triangles are a subset of the borehole array stations closest to the horizontal wells, and x symbols at the wells are the locations of the stages. Well C was the first to be stimulated, with hydraulic-fracturing treatments taking place along its full length. Features delineated by the microseismic activity are annotated: the large, N-S trending fault, NS1, runs roughly 500 m to the west of Well C, while a smaller N-S fault NS2 is closer to Well C. Five discrete clusters trending N30°E (SW1–SW5) extend east and west of Well C. Dashed magenta lines show the extrapolation of these features to NS1. The *SHmax* direction (top left) is inferred to be in the range of 45–60° (see section 2.4).

that are directly linked to subsequent HF stages from aftershock sequences that persist due to interevent triggering (e.g., Magshoudi et al, 2018) without any further anthropogenic contribution.

### 2.1. Event Detection and Hypocenter Location

The initial data acquisition and processing is described in detail by Eaton et al. (2018), and briefly reviewed here. Event detection was performed using an amplitude-based triggering algorithm to identify a set of template events. A matched-filter approach (e.g., Caffagni et al., 2016) was then used to detect smaller events with waveforms similar to the templates. A relatively low detection threshold was used, with the emphasis being avoidance of missed detections. After manual quality control to remove false positives, this produced a catalog of over 25,000 putative events. Eaton et al. (2018) used a relative location method to compute event hypocenters, but low signal-to-noise ratios meant that only 4,083 events could be robustly located. The

benefit of using this method is that key features were highlighted, with uncertainties in relative location of less than 50 m in map view and less than 100 m in depth view (N. Igonin et al., 2018).

All of the events located with the relative location method had moment magnitudes >−0.5. The initial processing therefore failed to capture events that are directly associated with hydraulic fracturing, which have a typical magnitude range of −3 to −0.5 (Eaton, 2018). To improve the magnitude of completeness and gain a better understanding of the event sequences, we used the short-time/long-time averaging (STA/LTA)-based beamforming approach described by Verdon et al. (2017) to locate additional events. A velocity model derived from a nearby vertical well was used to calculate hypocenter locations. Applying quality-control criteria based on the observed stacking power, as described by Verdon et al. (2017), we successfully located 18,472 events (Figure 2). This catalog has over 10 thousand events between magnitude −2 and 0, with a magnitude of completeness of −0.2. The improvement in event detection resulted in a significant increase in the detail provided by the microseismic observations.
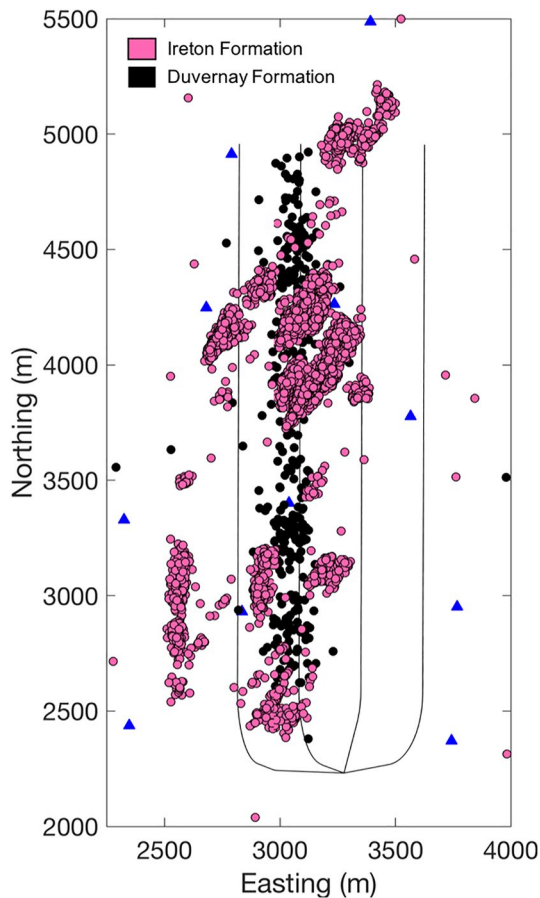
### 2.2. Event Locations

A map of 18,472 located events is shown in Figure 2. The colored circles correspond to the events that occurred during the stimulation of Well C, while the gray dots represent events that occurred during the subsequent stimulation of Wells A, B, and D. There were 125 stages completed during hydraulic fracturing of Well C, with an average injection volume per stage of 500 m³. The hydraulic-fracturing stimulation program proceeded from the toe of Well C (i.e., the northernmost end) to the heel. An *animation* of the seismicity sequence is provided in the online Supplementary Materials.

Microseismicity that is directly linked to hydraulic-fracture propagation, known as operationally induced microseismicity (Eaton, 2018), occurs during (or shortly after) active injection stages. Such events are generally characterized by subzero moment magnitudes and typically form elongate clusters aligned parallel to the maximum principal stress direction, *SHmax*, tracking the propagation of hydraulic fractures (Eaton, 2018). Based on the design of the hydraulic-fracturing stimulation in this study, we expect to see biwing hydraulic-fracturing events within ∼200 m of each stage in a symmetrical distribution in both directions. However, due to the magnitude of completeness for the monitoring array, many of the stages appear to have limited associated microseismicity. In particular, the first 20 stages have few events within the immediate vicinity of the wells. Instead, two structures are illuminated by the microseismicity during this time, which are oriented at N30°E, oblique to the regional *SHmax* orientation (N45°E–N60°E, see section 2.4). These two features appear to be mutually aligned and are labeled as SW1 in Figure 2 (South-West striking fracture network 1). Both SW1 clusters extend up to 600 m away from the well, which is significantly farther than normally anticipated for hydraulic fracturing (Maxwell et al., 2010). As the hydraulic-fracturing stages proceeded southwards along the well, the locus of microseismicity migrated along this structure, moving progressively to the southwest.

This same behavior is apparent along another four structures, all of which are parallel, striking at N30°E (labeled SW2–SW5). For each of these structures, microseismicity initiated in the northeast and propagated to the southwest as the active hydraulic-fracturing stages moved southwards along the well. This spatiotemporal evolution is inconsistent with expectations for operationally induced microseismicity, which generally initiates at the well and migrates outwards (Eaton, 2018).

Another significant feature is located approximately 500 m west of Well C. This structure (NS1: north-south fault 1) is oriented at N5°E, and ultimately grew to become a 1.5 km long lineation. All of the largest-magnitude events occurred along NS1. A smaller north-south trending structure, NS2, is also apparent toward the south end (heel) of Well C. This feature appears to intersect the inferred SW5 structure.

In the second half of the stimulation program, Wells A, B, and D were hydraulically fractured concurrently, with stages alternating between the wells and progressing from north to south. During this part of the program, the SW1–SW5 features were *reactivated*, in addition to several more NE-SW-trending features further to the east. The northern portion of NS1, which was quiescent during stimulation of Well C, also experienced activity during the stimulation of Wells A, B, and D. However, these events in the northern portion

**Figure 3.** Locations of inferred hydraulic-fracturing events (black circles) and induced seismic events (pink circles). The depths of the HF events place them within the targeted Duvernay Formation, but other events (possibly induced) are shallower, and occur within the overlying Ireton Formation.

of NS1 are not the focus of our study, since our objective is to examine how this linear feature, inferred to be a fault, was initially activated by hydraulic-fracturing operations.

### 2.3. Interpretation of Key Structures

To further investigate the key structures described above, we consider the Gutenberg-Richter $b$-values of magnitude-frequency distributions, event focal mechanisms, the seismicity depth distribution, event locations, and occurrence times relative to active injection stages.

The linear NS1 feature is interpreted as a strike-slip fault. This cluster hosts the largest events, with magnitudes up to $M_W$ 3.2 and right-lateral strike-slip mechanisms (Zhang et al., 2019). Based on a maximum-likelihood estimate of the slope of the magnitude-frequency distribution ($b$ value), N. Igonin et al. (2018) estimated that $b \sim 1.1$ for events along this feature. Cases of $b \sim 1$ may be indicative of the release of tectonic stresses on a large, planar structure (e.g., Kettlety et al., 2019; Urbanic et al., 1999; Verdon & Budge, 2018; J. P. Verdon et al., 2013). Taken together with the overall length of NS1 (>1.5 km), we interpret this as a preexisting fault that was sequentially activated during hydraulic fracturing. Similarly, seismicity along NS2 is characterized by $b \sim 1.1$ (N. Igonin et al, 2018); based on this $b$ value and its strike direction parallel to NS1, we infer that NS2 is likely to be a smaller fault that is related to NS1.

For both NS1 and NS2, careful analysis of focal depths of the associated seismicity (in the supplementary material) shows that many of these events are located within the Ireton shale, above the target Duvernay Formation (Figure 3). Event depths were determined using the focal-time method, a new technique that correlates arrival-time picks with 3D multicomponent (converted-wave) seismic observations (Poulin et al., 2019). In cases where 3-D multicomponent seismic observations are available, this method leverages unambiguous time-depth information derived from well ties and correlation of reflections observed in the P-P and P-S seismic datasets (Poulin et al., 2019).

The seismicity associated with the SW1–SW5 structures is also depth-located within the overlying Ireton Formation (Figure 3), although a small subset of these events is located in the Duvernay Formation. Within-zone events also occur along the track of Well C, in spatial and temporal proximity to the corresponding injection stage. We infer that this event subset, within the target formation and near the injection point, is operationally induced microseismicity that is directly associated with hydraulic fracturing. We expect such microseismicity to have relatively low magnitudes, which limits the number of these events that are detectable; hence details such as hydraulic-fracture orientation are difficult to discern clearly.

We now turn our attention to the SW1–SW5 structures. In Figure 3, event populations are colored according to whether hypocenters are located in the Duvernay (black) or the overlying Ireton Formation (pink). The SW structures are primarily concentrated in the Ireton shale, above the hydraulic-fracturing zone. The estimated $b$ values for the SW clusters are $b \sim 2.54$ for the NE portion of SW1, $b \sim 2.18$ for the SW portion of SW1, and $b \sim 1.82$ for SW2, SW3, and SW4 combined (N. Igonin et al., 2018). Fault activation is associated with $b$ values of approximately 1, while activity on fracture networks and on hydraulic fractures is often associated with $b$ values of two or more (e.g., Urbancic et al., 1999; J. P. Verdon et al., 2013). Since the SW structures have elevated $b$ values, this is further evidence that may be indicative of seismicity driven by fluid pressure perturbations within distributed fracture networks. Both operational microseismicity and microseismicity along fracture networks would be expected to have elevated $b$ values ($\geq 2$), so further evidence is required to differentiate the two kinds of seismicity.

There are several observations that indicate that the SW1–SW5 clusters of seismicity are not directly related to hydraulic-fracture growth. First, their orientation at N30°E is oblique (by 15–30°) to *SHmax* (see section 2.4), the expected orientation of seismicity clusters that form near hydraulic fractures (Eaton, 2018). Second, the majority of event depths are above the stimulation zone, contrary to expectations for operationally induced microseismicity. Moreover, these zones were reactivated during subsequent stimulation in Wells A, C, and D, which is not generally observed during hydraulic fracturing. Finally, hydraulic fractures initiate at the well and grow outwards, whereas the observed pattern of seismicity exhibits retrograde behavior, initiating in the northeast and migrating toward the well (see animation in supplementary material). Collectively, these lines of evidence indicate that seismicity within clusters SW1–SW5 is not directly related to hydraulic-fracture growth. Given their elevated *b* values, our preferred interpretation is that these features represent distributed fracture corridors (e.g., Peacock et al., 2016; Questiaux et al., 2010), rather than simple planar faults.

Our observations indicate that preexisting natural fracture systems in the overlying Ireton Formation were activated by pressure increases caused by hydraulic fracturing in the Duvernay Formation. Since the Ireton Formation is more brittle than the Duvernay Formation (Fox & Soltanzadeh, 2015), it is more likely to preserve natural fractures. This relationship is consistent with a structural model for the ToC2ME site, proposed by Eaton et al. (2018), in which the four HF wells are located in a flower structure that formed during the Devonian within a step-over zone between basement-rooted strike-slip faults. A regional flower-structure model has also been proposed to explain patterns of induced seismicity in other nearby studies of hydraulic fracturing in the Duvernay Formation (Eyre et al., 2019; Wang et al., 2018). Flower structures often contain internal fracture systems (Riedel shears) that are oblique to the primary strike-slip faults (Hennings et al., 2012; Huang & Liu, 2017). We remark that the orientation of the linear event distributions in SW1-5 is also oblique, by approximately 15–30°, from the *SHmax* direction (45–60°). Taken together, this means that such fractures may be critically stressed, a condition that is conducive to fluid flow (Rogers, 2003).

## 2.4. Principal Stress Direction

On a regional scale in Alberta, there is a generally uniform maximum horizontal stress direction of *SHmax* ∼ 45° (Heidback et al., 2016). However, in the vicinity of the ToC2ME program, the *SHmax* orientation could be as high as 60° (Zhang et al., 2019). One of the likely reasons for this variability is proximity to carbonate platforms, which have been shown in previous studies to have a significant control on the stress field orientation (e.g., Viegas et al., 2018). Since our dataset was acquired within a few kilometers of known reef/platform edges, additional data was used to determine the local stress conditions.

Zhang et al. (2019) computed focal mechanisms for 530 events of the ToC2ME dataset, a subset of which are shown in Figure 4. For the events in clusters NS1 and NS2 they found right-lateral strike-slip mechanisms, with one of the nodal planes oriented N-S, while for the events in the SW1–SW5 clusters they found right-lateral strike-slip mechanisms with one of the nodal planes oriented at 30°. The nodal plane strikes are consistent with the orientations of observed event clusters. Zhang et al. (2019) used these focal mechanisms to estimate the in situ stress field using a linear stress inversion method (Michael, 1984), finding *SHmax* ≈ N60°E. This value is up to 15° from the regional stress direction, but is consistent with the nearest in situ observation and within the range of WSM stress orientations observed in the local area, which is 59°. Taking into consideration the regional direction and uncertainty in the inversion, we infer that the *SHmax* direction is likely between 45 and 60°, acknowledging that the proximity to the reef edges may add local complexity to the stress field.

We do not observe clusters of microseismicity that are aligned parallel to the *SHmax* direction, which is the expected orientation for operationally induced microseismicity during hydraulic fracturing (e.g., Eaton, 2018). The focal mechanisms provide further evidence for an interpretation that the SW-trending clusters represent the reactivation of preexisting fracture zones. The events along the SW features consistently show right-lateral strike-slip mechanisms. If these events were delineating the propagation of new hydraulic fractures, then as well as requiring an unexpected *SHmax* orientation (i.e., 30°),
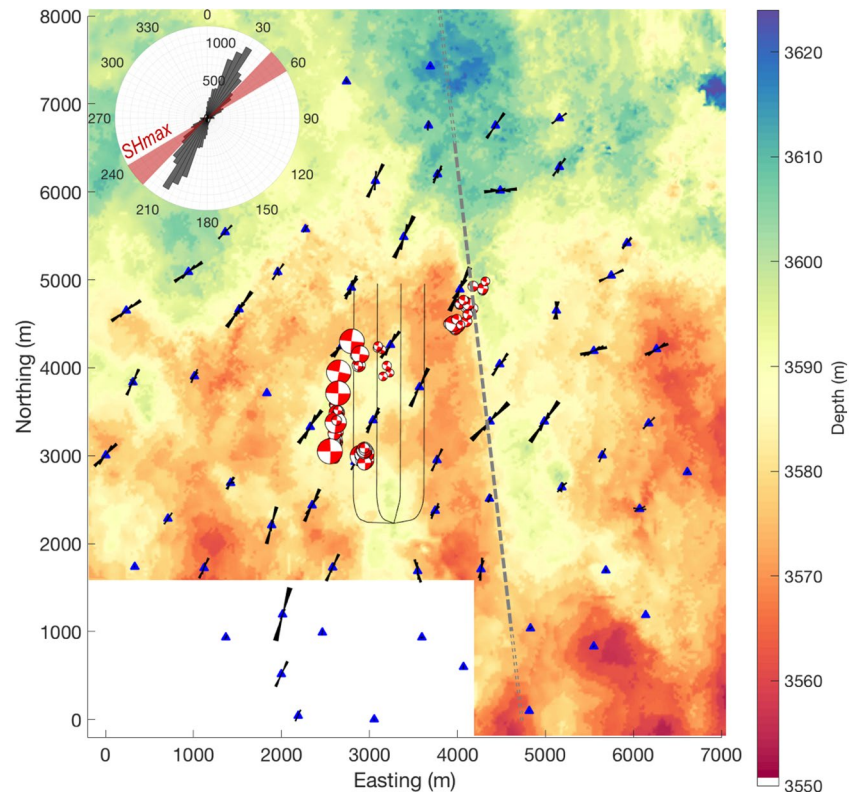
**Figure 4.** Map view of anisotropy observed using *S* wave splitting analysis. Fast *S* wave directions are plotted as rose diagrams at each station and focal mechanisms for the 100 largest events (Zhang et al., 2019) are shown at their respective event locations. The inset shows the aggregate measurements compared to the *SHmax* range. Background contours show the depth structure of the Beaverhill Lake Group formation based on 3-D seismic data and gray dashed lines indicate the extent of a fault to the east of the wells from seismic mapping (Eaton et al., 2018).

previous studies suggest that a mixture of different mechanisms would be expected in the case of operationally induced events (e.g., Baig & Urbancic, 2010). The apparent prevalence of right-lateral strike-slip faulting within these clusters demonstrates that the maximum stress orientation must be clockwise of (i.e., higher than) the 30°strike of these features, and therefore that these features do not follow *SHmax*, and cannot represent the propagation of new hydraulic fractures. As described above, we infer that most of the microseismicity that would be directly associated with hydraulic fracturing falls below the detection limits of the methods used here. In contrast, hydraulic fractures intersect faults or fracture corridors this gives rise to larger, detectable events, with both the cluster orientation and the focal mechanisms aligned along the orientation of the activated feature.

Given the range of estimated *SHmax* orientations of 45–60°, the optimal orientation for failure is 15–30° assuming a typical friction coefficient of 0.6. Consequently, the N5°E faults are likely misoriented by 10° or more, regardless of which *SHmax* direction is correct. There are other documented examples of misoriented faults that have been activated by fluid injection (Cochran et al., 2020; Healy et al., 1968; Skoumal et al., 2019), for reasons that remain poorly understood. It is also possible for exceptionally weak faults to be activated despite being at a high angle to *SHmax* (e.g., Townend & Zoback, 2004). Similarly, *SHmax* orientation may be perturbed in the vicinity of a fault due to strength heterogeneity (de Joussineau et al., 2003). Such lateral strength heterogeneity could arise, for example, due to proximity to massive carbonate reef structures, which are large, mechanically strong bodies located <1 km from the well head (Weir et al., 2017). In the following section, seismic anisotropy is used to explore whether key features in this dataset can be identified based on the fast *S* wave polarization direction and whether there is any associated indication of a stress heterogeneity.

### 2.5. Imaging Fracture Networks Using Seismic Anisotropy

Seismic anisotropy can be measured from the magnitude and direction of shear wave splitting observed using waveforms. The magnitude of the seismic anisotropy (time difference between fast and slow arrivals) signifies the strength of the anisotropy averaged along the raypath through the anisotropic media. The direction of seismic anisotropy, or the fast $S$ wave polarization, may be influenced by two factors: (1) stress direction (i.e., $SHmax$), and (2) subsurface structural fabric. To image the seismic anisotropy at the ToC2ME site we used the method of Teanby et al. (2004) to measure $S$ wave splitting on the 300 largest-magnitude events, since these had the best signal-to-noise ratios and clear $P$ and $S$ wave picks on all or most stations. We made >20,000 individual $S$ wave splitting measurements (300 events recorded at 69 stations), but quality-control criteria (Teanby et al., 2004) reduces this to a population of 7,818 good quality measurements.

The path-average fast $S$ wave orientations, $\Psi$, are plotted at each receiver in Figure 4. Coherent spatial variation in $\Psi$ is evident over the array footprint, with $\Psi$ oriented N-S to the south east of the array but more E-W to the NE of the array. In the vicinity of the wells, $\Psi$ is relatively consistent with a fast direction of $\sim30°$. This is aligned with the orientations of the SW1 – SW5 clusters, but is rotated $\sim30°$ counterclockwise from the estimated $SHmax$ orientation of N60°E (Zhang et al., 2019) and 15° counterclockwise from the regional $SHmax$ orientation of N45°E. These relationships suggest that the fast $S$ wave direction of $\Psi \sim 30°$ is strongly influenced by the orientation of fractures within the Ireton formation. Since they make an estimated angle of 15–30° from $SHmax$, these inferred parallel fracture sets would be close to optimally oriented for failure given typical friction coefficient values (Zoback & Kohli, 2019). Since the fast $S$ wave direction is influenced by both $SHmax$ and subsurface structure, the two cannot be definitively separated. Although we propose that the fast $S$ wave direction is more strongly influenced by the 30° inferred fracture networks, it is possible that the subtle clockwise rotation of the fast $S$ wave direction in Figure 4 may also be indicative of a slight rotation of the $SHmax$ direction in this area.

A 3D multicomponent reflection seismic survey acquired at the site provides further information about faults at the site. Figure 4 shows the depth to the top of the Beaverhill Lake Group formation, which immediately underlies the Duvernay. Significant depth discontinuities mark the positions of dip-slip faults that extend from the Precambrian basement through to the Duvernay (Eaton et al., 2018). In particular, a large fault trending roughly N-S can be seen just to the east of Well A, thought to have initially formed during extensional rifting in the Precambrian (Ekpo et al., 2017). However, this feature does not appear to have been reactivated during injection. No clear structure associated with the NS1 fault can be seen in the 3D seismic; this is not surprising, since this is most likely a near-vertical, strike-slip fault, which would not produce detectable offset of horizontal strata. Similar reactivation of faults that are not detectable with 3D seismic data has been documented elsewhere (e.g., Clarke et al., 2019).

Based on 3-D seismic data (Eaton et al., 2018), the observed faults are interpreted to be basement rooted (i.e., they extend downwards into the Precambrian basement). However, there is no indication of seismicity extending into the basement (see supplementary material). This behavior contrasts with induced earthquakes in Oklahoma and Ohio, where the largest earthquakes have been shown to occur in the basement, both due to wastewater injection (Ellsworth, 2013), and hydraulic fracturing (Kozłowska et al., 2018).

## 3. Interpretation: Position and Timing of Fault Reactivation

We investigate fault-activation processes by examining the timing and position of reactivation within the various clusters relative to positions of HF stages. Figure 5 shows a detailed view of the seismicity associated with the SW2–SW4 structures, from stages 30–80 of Well C. In addition to the observed microseismic events, we plot ellipses with long axes oriented at 60°, centered on each perforation interval. These are included to highlight the assumed extent of the hydraulic-fracture zones, which are not clearly imaged by the microseismic events. The timing of these sequences of microseismicity is also listed in Table 1.

Seismicity on SW2 began at approximately 23:00 on the 2 November 2016. Activity began on the SW3 structure at 18:00 on 4 November 2016. The first events on the NS1 fault were also seen shortly afterward, at 20:00 on 4 November 2016. The positions of the first events on NS1 are aligned with the SW2 cluster, i.e., they occur at the point where linear extrapolation of the SW2 cluster intersects the NS1 fault (as shown by the
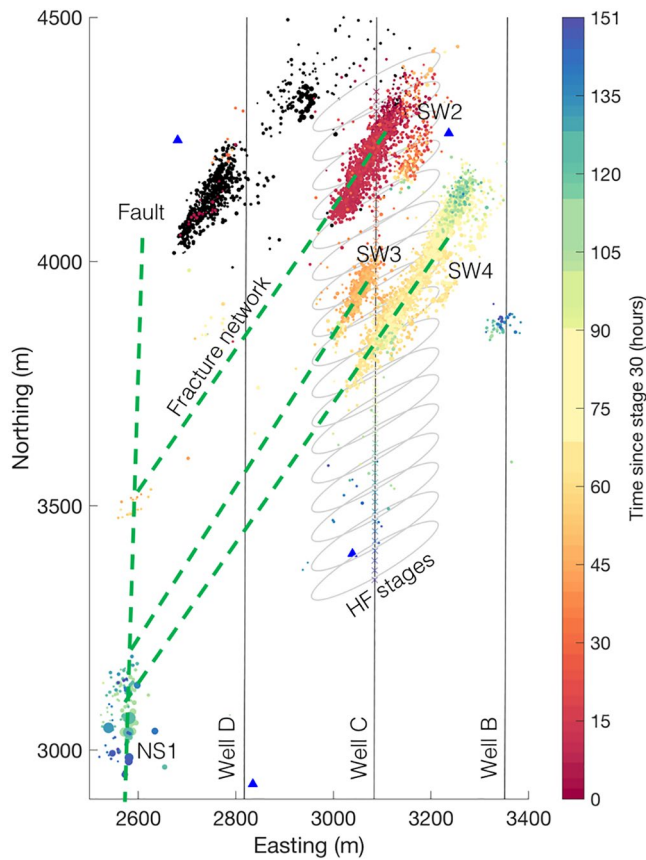
**Figure 5.** Snapshot of activity along Well C between stages 30 and 80. Colored dots show events that occurred during the specified time period and black dots show previous events. Dashed green lines highlight interpreted fault corridors at N30°E. The gray ellipses schematically depict the likely extent of hydraulic fractures, which trend parallel to *SHmax* and have a half-length of 150 m. The x symbols along the well indicate the position of the stages.

green dashed lines in Figure 5). The lateral distance from the active stage at this time, Stage 48, to the first NS1 events is approximately 800 m; in addition, these NS1 events do not align with a continuation of the Stage 48 position along the *SHmax* direction.

As stimulation proceeded, activity continued in the SW3 cluster and began in the SW4 cluster as it was intersected by the stimulation zones at 07:00 on 5 November 2016. At 10:00 on 7 November 2016, activity renewed on the NS1 fault, with events located several hundred meters south of the first events. The new locus of activity on NS1 is aligned with the SW3 feature and is approximately 900 m from the position of the active stage. Once again, the events on the NS1 fault do not align with a continuation along the *SHmax* direction of the synchronous active stage, but occurred in a position at which linear extrapolation of one of the SW clusters intersects the NS1 fault. By 03:00 on the 9 November 2016, the loci of seismicity had again shifted southwards on the NS1 fault, to a position aligned with the SW4 cluster.

The same pattern of behavior is observed as stimulation reaches the southernmost SW5 cluster. This feature appears to have been activated when it was intersected by the hydraulic stimulations at 18:00 on the 8 November 2016. Activity on the smaller NS2 fault began where it intersects the SW5 cluster at 23:00 on 9 November 2016. Further activity is observed on the NS1 fault, at a position that is in alignment with the SW5 structure, at 20:00 on the 12 November 2016. The animation in the supplementary material further illustrates this behavior.

We conclude that the timings and positions of the seismicity on the NS1 fault are consistent with a model wherein fault activation is controlled by the positions of intersections of the SW-trending fracture corridors with the fault. When the NS1 fault was initially activated, it did so in a position that is directly aligned with the SW2 cluster (Figure 2). Subsequently, the loci of activity shifts southwards along NS1, where each shift in position was aligned with each of the SW clusters in space. We therefore postulate that the SW2–SW5 fracture corridors represent permeable pathways, transmitting elevated pore pressures from the well to the NS1 and NS2 faults. There is a time delay of 44–98 h between the activation of each SW cluster at the well and the occurrence of seismicity at the corresponding

**Table 1**
*Sequence of Processes That Occur During the Stimulation, as Illuminated by the Microseismicity*

| Time | Stage no. | Processes |
|---|---|---|
| October 31, 23:00 | 7 | Activity begins in SW1 cluster |
| November 2, 23:00 | 29 | Activity begins in SW2 cluster |
| November 4, 18:00 | 47 | Activity begins in SW3 cluster |
| November 4, 20:00 | 48 | Activity begins on the NS1 fault, at a position in line with the SW2 cluster |
| November 5, 07:00 | 53 | Activity begins in the SW4 cluster |
| November 7, 10:00 | 64 | Activity on the NS1 fault shifts southward to a position in line with the SW3 cluster |
| November 8, 18:00 | 73 | Activity begins in the SW5 cluster |
| November 9, 03:00 | 77 | Activity on the NS1 fault shifts southward to a position in line with the SW4 cluster |
| November 9, 23:00 | 87 | Activity begins on the NS2 fault where it is intersected by the SW5 cluster |
| November 12, 20:00 | 115 | Activity on the NS1 fault shifts southward to a position in line with the SW5 cluster. |

**Table 2**
*Delay Times Between the Onset of Activity in Each of the SW Clusters, and the Onset of Activity on the Corresponding Segments of the NS1 Fault*

|  | Time activation begins at well | Time activation on corresponding part of NS1 begins | Time delay (h) |
|---|---|---|---|
| SW1 | October 31, 23:00 | NA | NA |
| SW2 | November 2, 23:00 | November 4, 20:00 | 44 |
| SW3 | November 4, 18:00 | November 7, 10:00 | 64 |
| SW4 | November 5, 07:00 | November 9, 03:00 | 92 |
| SW5 | November 8, 18:00 | November 12, 20:00 | 98 |

position on NS1 (see Table 2). This time delay may correspond to the time elapsed as elevated pressures diffused along the SW-trending fracture corridors, reaching and reactivating the NS1 fault. The distribution of microseismic events observed along the SW2–SW5 clusters does not extend as far as the NS1 fault. Our interpretation is that the pore-pressure perturbation is communicated, in part, aseismically, or at least without generating seismic events above the detection limits of the monitoring array.

In summary, the foregoing observations and discussion lead to the following interpretive classification scheme:

1. Fault activation (NS1, NS2): characterized by a *b* value of ~1, occurrence of large events, and large, linear structure.
2. Fracture network activation (SW1–SW5): characterized by *b* values ~2, temporal evolution of events along the structure from NE to SW (rather than growth outwards from the well), focal mechanisms not consistent with HF, apparent misalignment with *SHmax*, and depth above the zone of interest.
3. Operational microseismicity: characterized by occurrence during injection and focal depths within the zone of interest.

In the following section, we apply this classification scheme to test whether the primary mechanism for fault activation along NS1 is pore-pressure perturbation or static stress changes.

## 4. Investigating Possible Mechanisms for Fault Reactivation

In the preceding sections, we presented evidence that fracture networks may provide conduits for pressure perturbation that leads to fault activation. To test the feasibility of this mechanism, we generate simple representative models for this scenario. Our objective is not to provide a definitive constraint on the properties of the fracture corridors, but simply to show that reasonable values for the corridor's dimensions and flow properties can generate plausible perturbations at the fault, both in terms of the time at which the perturbation arrives, and the magnitude of the perturbation. For comparison, we also discuss the possibility of event triggering through poroelastic stress transfer, and by static stress transfer between the events observed on the SW2–SW5 clusters.

### 4.1. Fluid-flow modeling

To investigate whether fluid flow along preexisting fracture corridors is a plausible mechanism for fault reactivation, we model the expected diffusion of pressure along a fracture corridor. Initially we approach the problem analytically, using the concept of seismic diffusivity. Talwani and Acree (1985) studied a series of reservoir-impoundment induced earthquakes. Their observations of delay times between reservoir lake levels and seismicity, and of increasing epicentral areas with time, led them to conclude that pore-pressure diffusion was the causative mechanism. They developed the concept of seismic hydraulic diffusivity, $\alpha_s$, which describes the relationship between the event occurrence time *t*, and the distance between the event and the pore-pressure source *L*:

$$\alpha_s = \frac{L^2}{t}. \tag{3}$$

Along the 30° orientation mapped by the SW clusters, the NS1 fault is located roughly 800–1,000 m from Well C. The events on the NS1 feature commence from between 44 and 98 h after activation of each of the respective SW clusters (Table 2). Using these parameters in Equation (3), we arrive at values of $2.8 < \alpha_s < 7 \ \mathrm{m^2/s}$, well within the range of values described by Talwani and Acree (1985), who found values of $0.5 < \alpha_s < 60 \ \mathrm{m^2/s}$ for a variety of geological settings, with most values clustering around 5 $\mathrm{m^2/s}$.
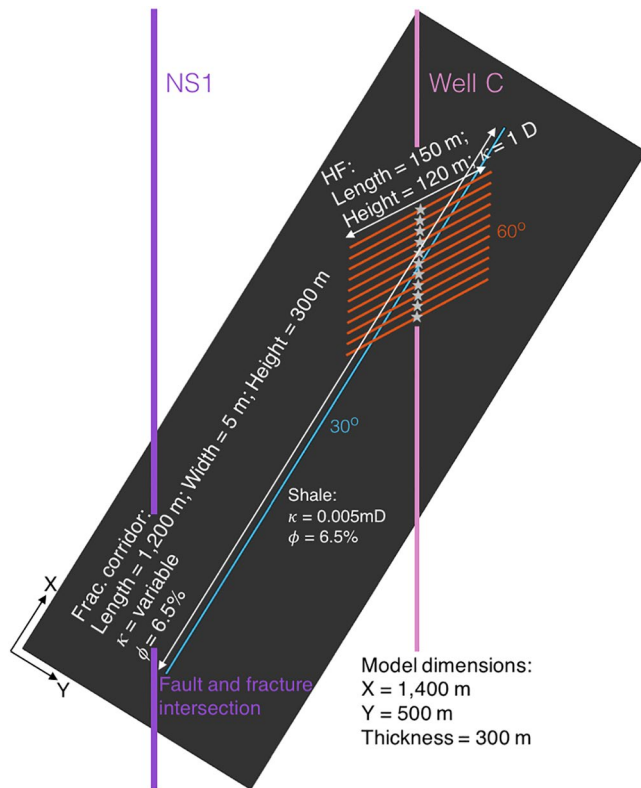
**Figure 6.** Schematic representation of our fluid-flow model: 11 HF stages (orange lines) are simulated, which connect into a fracture corridor (blue line) with a length of 1,200 m and a width of 5 m. The change in pore pressure is measured at the intersection of the fault (purple line) and fracture.

The permeability of a fracture corridor, $\kappa_{FC}$, can be computed from the diffusivity using (Brace, 1980):

$$\kappa_{FC} = \frac{\alpha_s \eta \phi}{K},\tag{4}$$

where $\eta$ is the fluid viscosity, $\phi$ is the porosity, and $K$ is the fluid bulk modulus. Because we do not know the properties of fluids that saturate the fracture corridors, we consider cases of both gas and water. We assume a porosity of $\phi = 6.5\%$ and use the Batzle and Wang (1992) equations to compute the properties of gas with a specific gravity of 1, and brine with a salinity of 100,000 ppm, at a temperature of 100 °C and a pressure of 38 MPa. These values are a very generic representation of conditions in the Ireton (e.g., Dunn et al., 2012; Lyster et al., 2017). Use of these values in Equation 4) yields an analytic solution with values of $\kappa_{FC}$ varying from 25 to 100 mD.

To incorporate greater complexity including multiple stages of injection at different times and locations we address the problem numerically using a commercial reservoir simulation code Tempest (Emerson, 2014). We create a model that represents our inferred system—hydraulic fractures intersecting a fracture corridor that transfers pressure increases—in a simplified form. Tempest simulates fluid flow through porous systems but does not simulate the coupled hydrogeomechanical behavior of HF propagation. Instead, we preinsert the hydraulic fractures and a fracture corridor into the model. This simplification is reasonable because our primary aim is to model fluid and pressure propagation along a preexisting fracture corridor, rather than to simulate the HF propagation itself. Whereas developing a hydrogeomechanical simulation is complex from a modeling perspective, reservoir fluid-flow models are relatively simpler to populate and utilize. Similarly, while in reality the permeability of a fracture corridor will be pressure-dependent, we do not simulate this effect in our model.

The model setup is shown in Figure 6. The background shale rock has a permeability of $\kappa_S = 0.005$ mD (Ghanizadeh et al., 2015a). We simulate 11 individual HF stages with a horizontal spacing of 20 m, representing roughly the number of stages that appear to be associated with reactivation of each SW-trending fracture corridor based on the observed microseismicity. Based on the operational records (Eaton et al., 2018), we model 400 m³ of water injected over a 3-h period for each stage, with a 1-h gap between each stage. Each stage connects to a HF with a permeability of 1,000 mD, a half-length of 150 m and a height of 120 m, running at 60° to the well trajectory. The fracture corridor to which the hydraulic fractures connect has a length of 1,200 m, and assumed width and a height of 5 and 300 m, respectively, running at 30° to the well trajectory. The fracture corridor is intersected by each of the hydraulic fractures that extend from the well. Using our analytical results as a starting point, we vary $\kappa_{FC}$ from 50 to 1,000 mD. Full model details are provided in the supplementary materials.

Figure 7 demonstrates an example model instantiation ($\kappa_{FC} = 100$ mD), showing the distribution of pore-pressure changes along the fracture corridor at a single model time step (an animation showing the pressure evolution along the fracture corridor as a function of time is provided in the online supplementary materials). Pressures become elevated where the active HF intersects the fracture corridor—this pressure pulse then propagates along the length of the fracture corridor.

Our primary interest is the pressure change at the distal end of the fracture corridor, where it intersects the NS1 fault. We are interested in the magnitude of the pressure increase and its timing relative to the injection stages, as this will indicate whether (i) the modeled pressure changes are sufficient to cause
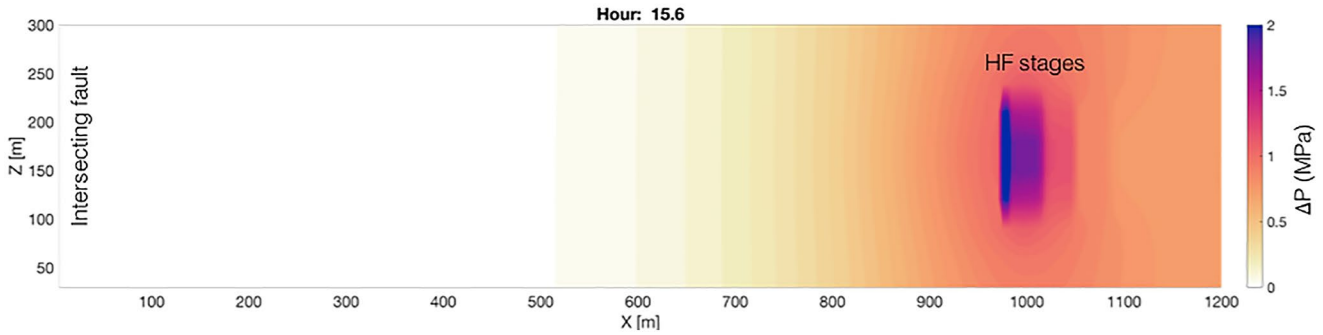
**Figure 7.** Modeled change in pore pressure (in MPa) at a single time step ($T = 15.6$ h) along the fracture corridor: pressures are elevated where the HF intersects the fracture corridor (at $X = 980$ m) and the pressure pulse thereupon propagates along the feature.

fault reactivation, and (ii) whether the timing of pressure increase is commensurate with the observed time delays between initial reactivation of the SW clusters near to the well and the onset of activity on the NS1 fault.

Figure 8 shows curves representing models with varying values of $\kappa_{FC}$. In each case, we observe an increase in pressure, the magnitude and timing of which is strongly dependent on the fracture corridor permeability. The magnitude of the pressure increase, $\Delta P_{MAX}$, is larger for higher permeabilities, with the largest increase
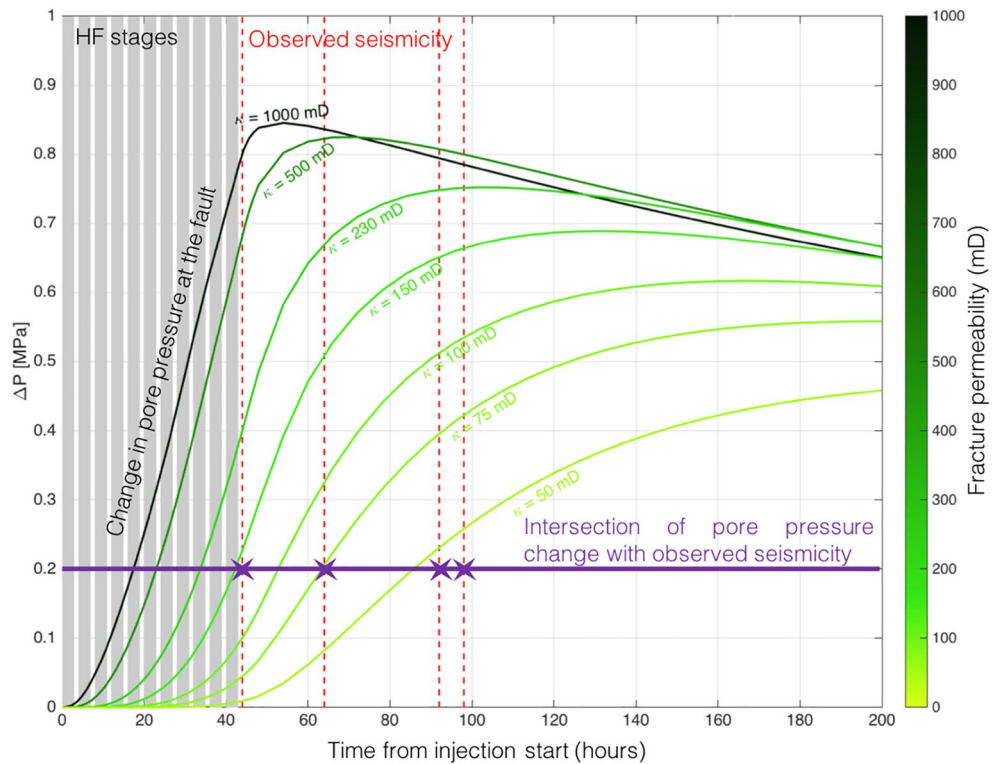


**Figure 8.** Modeled pore-pressure increases at the distal end of the fracture corridor as a function of time, for a suite of fracture corridor permeabilities from 50 to 1,000 mD. The 11 injection stages are marked by the gray shading, while the observed reactivation times of the NS1 fault from the onset of activity on each SW fracture corridor are marked by the red dashed lines. The green curves represent the change in pore pressure at the fault, at a lateral distance of 1 km, given the different values of fracture zone permeability. The horizontal purple line and purple stars indicate the intersection between an example pore-pressure change of 0.2 MPa at the fault and the observed seismicity.

of $\Delta P_{MAX} = 0.85$ MPa occurring for $\kappa_{FC} = 1{,}000$ mD, and the smallest increase of $\Delta P_{MAX} = 0.45$ MPa occurring for $\kappa_{FC} = 50$ mD.

This range of pressure increases is significantly larger than that modeled by Keranen et al. (2014) for the Jones, Oklahoma earthquake swarm, but is similar to that calculated by Schoenball et al. (2018) for the Guthrie-Langston, Oklahoma, earthquakes. It is also significantly larger than static stress transfer magnitudes that have been invoked as causes for fault activation elsewhere (e.g., Kettlety et al., 2020b; Pennington & Chen, 2017). Evidently, the range of pore-pressure increases produced by our model, regardless of $\kappa_{FC}$, are within (or above) the range typically deemed sufficient to cause fault reactivation.

The time delay between the start of injection and the maximum pressure increases at the distal end of the fracture, $T_{PMAX}$, is smaller for higher permeabilities, with the smallest delay time of $T_{PMAX} = 52$ h for $\kappa_{FC} = 1{,}000$ mD, and the largest delay time of $T_{PMAX} = 250$ h occurring for $\kappa_{FC} = 50$ mD. Once $\Delta P_{MAX}$ has been reached, pressures gradually decrease as fluids diffuse into the nonfractured shale rock mass.

In Figure 8, the pressure increases with time are compared with the observed time delays between the onset of activity in each SW cluster and activity in the corresponding portion of the NS1 fault (Table 2, red dashed lines in Figure 8). Consider an example pore-pressure change of 0.2 MPa at the fault (purple line in Figure 8). For the lower permeability cases ($\kappa_{FC} = 50$ mD and $\kappa_{FC} = 75$ mD), the changes in pore pressure after 40 h (the shortest observed reactivation delay time) are negligible. This would appear to rule out these lower $\kappa_{FC}$ models, since elevated pressures are not able to reach the fault by the time that it is observed to reactivate.

For the $\kappa_{FC} = 1{,}000$ mD case, pressures at the distal end of the fracture corridor increase rapidly, and have reached almost their maximum value by the shortest observed reactivation delay time (40 h). In this case, we would expect to have observed seismicity much sooner, but that is not the case. Moreover, the modeled pressures are decreasing by c. 90 h, corresponding to the largest observed reactivation delay time, which would appear to rule out these models since we would expect reactivation to occur while pressures are increasing. However, the higher permeability models cannot be ruled out entirely, as delays between the reactivation trigger and the resulting seismicity have been observed (e.g., van der Elst et al., 2013), implying that the time delay between the modeled increase in pressures along the fracture zone and the observed seismicity on the fault is caused by the gradual nucleation of rupture on the fault before observed seismicity takes place.

Based on these models, the midrange permeability models ($\kappa_{FC} = 150$–$230$ mD) show the best match to the observed reactivation delay times. Within this permeability range, the pressure has increased by $> 0.2$ MPa within 44 h (the shortest observed reactivation delay period) and is continuing to increase, reaching near to the maximum by 90–100 h (the longest observed reactivation delay periods). Although these permeabilities are several orders of magnitude larger than the matrix permeability of the Duvernay Formation, laboratory tests of the permeability of unpropped fractures in similar rocks show that fracture permeability can be as high as 1–3 Darcies (Ghanizadeh et al., 2015b).

In summary, both the analytical and numerical modeling demonstrates that the observed delay times are consistent with pore-pressure transfer along a fracture corridor, assuming permeability values that are consistent with observations of seismic hydraulic diffusivity made in a range of geological settings (Talwani & Acree, 1985). Numerical modeling indicates that pore-pressure increases of 0.5 MPa might reasonably be expected at the fault, assuming such a mechanism.

### 4.2. Stress Transfer

Deformation and slip around Well C produced by hydraulic fracturing will affect the stress field in the surrounding rocks. If this produces Coulomb Failure Stress (CFS) increases on the NS1 fault, then this stress transfer represents a viable alternative causative mechanism for the induced seismicity. There are two potential sources for stress transfer onto the NS1 fault. The first is elastostatic stress transfer due to the tensile opening of the hydraulic fractures (e.g., Kettlety et al., 2020b), and the second is static stress transfer by seismicity occurring in each of the SW clusters.
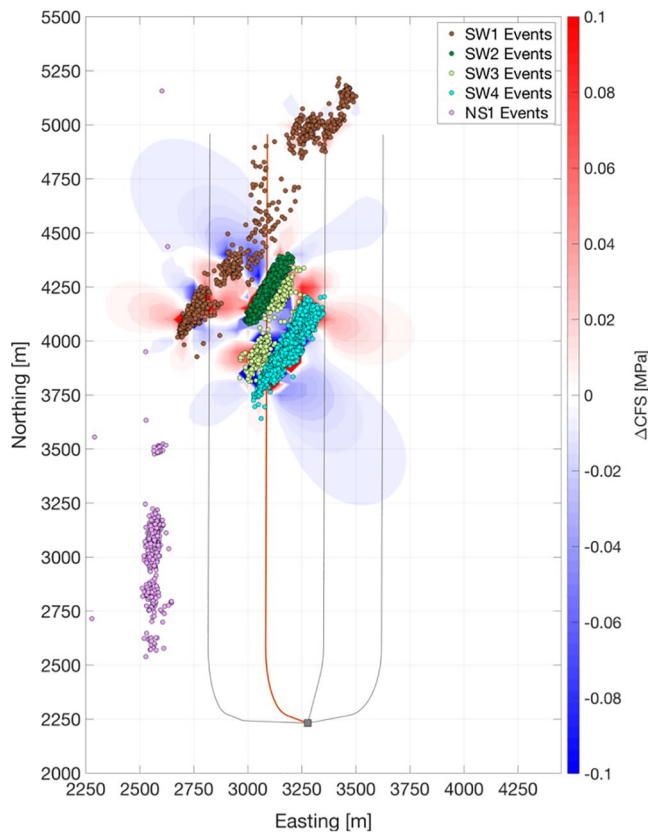
**Figure 9.** Changes in Mohr-Coulomb failure criteria (ΔCFS) produced by the slip of the events in the SW clusters, resolved onto the NS1 fault orientation. Here we show the cumulative stress change produced by all of the clusters. The impacts on the NS1 fault events (pink) are small, and actually lie within a lobe of negative ΔCFS.

### 4.2.1. Stress Transfer Caused by Tensile Hydraulic-Fracture Opening

Hydraulic fracturing occurred along the length of Well C from toe to heel using a very similar injection design for each stage. Hence, if stress transfer from tensile hydraulic-fracture opening was the cause of seismicity on the NS1 fault, then we would expect the fault to reactivate along its entirety, with the loci of seismicity moving consistently southwards along the fault. Instead, as documented in section 3, seismicity occurs at specific points along the fault that are aligned with the SW clusters.

The behavior of the NS1 fault during stimulation of Well C can be contrasted with the behavior during stimulation of Well D, which is within 200–300 m of the fault. During stimulation of Well D, the NS1 fault reactivates along its entire length, with the loci of seismicity moving consistently southwards as the hydraulic stimulation moves southwards along Well D, as might be expected if there is direct interaction between the hydraulic fractures and the fault.

Models of poroelastic stress transfer generated by tensile fracture opening (e.g., Kettlety et al., 2020b; Westwood et al., 2017) have found changes in the CFS at distances larger than 500 m to be significantly smaller than the pore-pressure changes modeled in section 4.1. For this reason, stress transfer effects due to tensile hydraulic fracture are unlikely to be to driving force of induced seismicity observed in this case study.

### 4.2.2. Static Stress Transfer by Events in the SW Clusters

An alternative possibility is that slip on the NS1 fault could have promoted interevent triggering through the mechanism of static stress transfer. Modeling of stress transfer caused by earthquake slip is well-established, having its origins in aftershock distribution after large tectonic earthquakes (e.g., Stein et al., 1992). Here we use the PSCMP code (R. Wang et al., 2006) to model the changes in CFS caused by the events in each of the SW clusters.

This modeling requires the rupture dimensions and orientation to be specified. Such parameters can only be directly constrained for a small fraction of the events with the highest signal-to-noise ratios (e.g., Zhang et al., 2019). Instead, we approach the problem from a stochastic perspective (e.g., Verdon et al., 2015). We know the position of each event, and the event magnitudes. We assign source mechanism parameters to each observed event in each cluster randomly from appropriate statistical distributions. We perform 1,000 model realizations for each of the SW clusters, taking as our result the median stress changes from the overall model population (following the method used by Kettlety et al., 2020b).

Zhang et al. (2019) show that all the events within the SW clusters have consistent right-lateral strike-slip mechanisms, with vertical nodal planes striking at 30° (parallel to the overall cluster orientations). We therefore assign nodal planes strikes with a normal distribution with a mean of 30° and a standard deviation of 5°, dips with a normal distribution with a mean of 90° and a standard deviation of 5°, and rakes with a normal distribution with a mean of 180° and a standard deviation of 5°. Stress drops are assigned with a uniform distribution ranging from $0.1 < \Delta\sigma < 10$ MPa, from which the rupture dimensions and displacement are computed using the event magnitude. We assume a Young's moduli of 50 GPa and a Poisson's ratio of 0.25, based on values for the Duvernay observed by Soltanzadeh et al. (2015) and Weir et al. (2017).

To determine the impact on the NS1 fault, we resolve the modeled stress changes into shear and normal stresses acting on a vertical, right-lateral strike-slip fault with a strike of 5°. The results of our stress modeling—the changes in the Mohr-Coulomb criteria (Equation 2)—are plotted in Figure 9. We observe that the

modeled stress changes are small, less than 0.01 MPa at the point where the first events on the NS1 fault are observed. Moreover, the events on NS1 lie within a lobe of negative CFS change, indicating that the stress changes move the NS1 feature away from, rather than toward, failure.

Our permeable corridor models suggest an increase in pore pressure of approximately >0.2 MPa at the fault, which would decrease the effective normal stress acting on the fault, pushing it toward failure. By comparison, the stress transfer modeling produces a negative CFS change of less than 0.01 MPa. Our preferred model is therefore pore-pressure transmission via a hydraulic connection, rather than by stress transfer between events transmitted through the rock frame.

### 4.3. Implications for Risk Assessment

Eaton et al. (2018) examined the 3D/3C reflection seismic data at this site. They were able to identify faults, but found that there was limited evidence for spatial correlation between faults imaged by the reflection seismic and features reactivated by the seismicity. For example, the NS1 fault on which the largest events occurred was not expressed in the reflection seismic data, whereas large faults near to the wells imaged by the reflection seismic (e.g., F2 and F6 of Eaton et al., 2018) showed no signs of reactivation. This implies that we cannot rely on predrill site selection using only the geometrical fault distance (e.g., Westwood et al., 2017) to mitigate induced seismicity, because faults that are imaged may not reactivate, while seismic events may occur on faults that were not imaged.

Since we cannot directly image all faults in the subsurface, we assume that critically stressed faults may be distributed throughout a given volume of rock. If this is the case, then the probability that a given industrial activity triggers seismicity will depend on the size of the rock volume that it perturbs. In low permeability, unfractured shale rocks, the volume of rock affected by hydraulic fracturing will be relatively small, and therefore the probability of intersecting a critically stressed fault is expected to be correspondingly low. However, in this study we show that the presence of preexisting permeable fracture networks may significantly increase the volume of rock that is affected by the hydraulic fracturing, increasing the likelihood of fault activation. Similar cases have been observed in the Exshaw Formation in Alberta, Canada, where Galloway et al. (2018) suggest that karst collapse along near-vertical faults served as a conduit for vertical pressure transfer, and in the Montney play in northeastern BC, where transverse faults appear to provide permeable corridors for pore-pressure communication between faults in a buried thrust belt (Riazi & Eaton, 2020).

Various methods can be used to image subsurface fracture networks. For example, aligned fractures will create seismic anisotropy that can be imaged by seismic reflection surveys (e.g., Hall & Kendall, 2003). Once wells have been drilled, fracture networks may be imaged by borehole imaging logs. Geomechanical reconstructions can also be used to simulate the expected fracture networks (e.g., Bond et al., 2013). However, we cannot be sure that such methods will positively identify faults and fracture networks that may be of concern.

## 5. Conclusions

Hydraulic fracturing-induced seismicity reflects a complex interplay between different mechanisms of stress transfer and the conditions in the subsurface. In this study, we show that hydraulic fracturing resulted in operationally induced seismicity, the activation of preexisting fracture networks and the activation of faults. Reactivation of a fault adjacent to the wells, with a strike length of at least 1.5 km, was likely initiated by transfer of fluid pressure along preexisting fracture networks, resulting in delayed activation over 1 km away from injection. These inferred fractures allowed the pressure pulse to propagate much further from the well than would be expected if the low-permeability shale rock were otherwise intact. Seismic anisotropy was shown to be a potentially useful tool in imaging fracture networks, with anisotropy close to the wells aligning with the observed 30° fracture networks.

Modeling of the fluid flow along the fracture networks demonstrates the ability of the fracture networks to transmit sufficient changes in pore pressure to the fault at the observed distances. By matching the timing

of the observed seismicity along the fault to the pore-pressure increase, an approximate permeability is obtained that falls within an order of magnitude of permeability values from laboratory results. An observational argument allowed for the exclusion of poroelastic effects as a dominant force to explain our observations, and modeling of the Coulomb stress change showed that the events themselves produce insufficient stress change to trigger activity along the fault.

The approach used in this paper could be used to aid in the mitigation and interpretation of other cases of hydraulic fracturing-induced seismicity. The steps taken to differentiate types of seismicity in this dataset may be applied to other datasets, and the methods can be adapted to real-time monitoring. A pro-active approach with a traffic light system and flexibility with the stimulation program are key to mitigating induced seismicity in areas of suspected permeable fracture networks.

## References

Atkinson, G. M., Eaton, D. W., Ghofrani, H., Walker, D., Cheadle, B., Schultz, R., et al. (2016). Hydraulic fracturing and seismicity in the Western Canada Sedimentary Basin. *Seismological Research Letters*, *87*, 631–647.

Atkinson, G. M., Eaton, D. W., & Igonin, N. (2020). Developments in understanding seismicity triggered by hydraulic fracturing. *Nature Reviews*, *1*, 1–14. https://doi.org/10.1038/s43017-020-0049-7

Baig, A., & Urbancic, T. (2010). Microseismic moment tensors: A path to understanding frac growth. *The Leading Edge*, *29*(3), 320–324.

Bao, X., & Eaton, D. W. (2016). Fault activation by hydraulic fracturing in Western Canada. *Science*, *354*, 1406–1409.

Batzle, M., & Wang, Z. (1992). Seismic properties of pore fluids. *Geophysics*, *57*, 1396–1408.

Bond, C. E., Wightman, R., & Ringrose, P. S. (2013). The influence of fracture anisotropy on $CO_2$ flow. *Geophysical Research Letters*, *40*, 1284–1289. https://doi.org/10.1002/grl.50313

Brace, W. F. (1980). Permeability of crystalline and argillaceous rocks. *International Journal of Rock Mechanics, Mining Science and Geomechanics*, *17*, 241–251.

Caffagni, E., Eaton, D. W., Jones, J. P., & Van der Baan, M. (2016). Detection and analysis of microseismic events using a Matched Filtering Algorithm (MFA). *Geophysical Journal International*, *206*, 644–658.

Clarke, H., Eisner, L., Styles, P., & Turner, P. (2014). Felt seismicity associated with shale gas hydraulic fracturing: The first documented example in Europe. *Geophysical Research Letters*, *41*, 8308–8314. https://doi.org/10.1002/2014GL062047

Clarke, H., Verdon, J. P., Kettlety, T., Baird, A. F., & Kendall, J.-M. (2019). Real time imaging, forecasting and management of human-induced seismicity at Preston New Road, Lancashire, England. *Seismological Research Letters*, *90*, 1902–1915.

Cochran, E., Skoumal, R. J., McPhillips, D., Ross, Z. E., & Keranen, K. M. (2020). Activation of optimally and unfavorably oriented faults in a uniform local stress field during the 2011 Prague, Oklahoma, sequence. *Geophysical Journal International*, *222*(1), 153–168.

Darold, A., Holland, A. A., Chen, C., & Youngblood, A. (2014). Preliminary analysis of seismicity near Eagleton 1-29, Carter County. *Oklahoma Geol. Surv. Open-File Rep. OF2-2014*.

de Joussineau, G., Petit, J. P., & Gauthier, B. D. (2003). Photoelastic and numerical investigation of stress distributions around fault models under biaxial compressive loading conditions. *Tectonophysics*, *363*(1–2), 19–43.

Deng, K., Liu, Y., & Harrington, R. M. (2016). Poroelastic stress triggering of the December 2013 Crooked Lake, Alberta, induced seismicity sequence. *Geophysical Research Letters*, *43*, 8482–8491. https://doi.org/10.1002/2016GL070421

Dunn, L., Schmidt, G., Hammermaster, K., Brown, M., Bernard, R., Wen, E., et al. (2012). *The Duvernay Formation (Devonian): Sedimentology and reservoir characterization of a shale gas/liquids play in Alberta* (Article 90174). Calgary: Canada GeoConvention.

Eaton, D. W. (2018). *Passive seismic monitoring of induced seismicity: Fundamental principles and application to energy technologies*. Cambridge, UK: Cambridge University Press.

Eaton, D. W., Igonin, N., Poulin, A., Weir, R., Zhang, H., Pellegrino, S., & Rodriguez, G. (2018). Induced seismicity characterization during hydraulic fracture monitoring with a shallow-wellbore geophone array and broadband sensors. *Seismological Research Letters*, *89*, 1641–1651.

Ekpo, E. (2020). Geophysical constraints on basement faulting in west-central Alberta: Implications for induced seismicity and post-collisional modification of western Laurentia (*PhD thesis*). Calgary, Canada: University of Calgary.

Ekpo, E., Eaton, D., & Weir, R. (2017). Basement tectonics and fault reactivation in Alberta based on seismic and potential field data. In A. Okiweli (Ed.), *Geophysics*. London: Intechopen.

Ellsworth, W. L. (2013). Injection-induced earthquakes. *Science*, *341* 1225942.

Emerson (2014). *Tempest reservoir engineering*. Retrieved from http://www.emerson.com/documents/automation/tempest-more-data-sheet-2014-en-82050.pdf on 03.08.2018

Eyre, T. S., Eaton, D. W., Garagash, D. I., Zecevic, M., Venieri, M., Weir, R., & Lawton, D. C. (2019a). The role of aseismic slip in hydraulic fracturing-induced seismicity. *Science Advances*, *5*, eaav7172.

Eyre, T. S., Eaton, D. W., Zecevic, M., D'Amico, D., & Kolos, D. (2019b). Microseismicity reveals fault activation before MW 4.1 hydraulic-fracturing induced earthquake. *Geophysical Journal International*, *218*, 534–546.

Fox, A. D., & Soltanzadeh, M. (2015). *A regional geomechanical study of the Duvernay formation in Alberta, Canada*. Calgary, AB: GeoConvention.

Friberg, P. A., Besana-Ostman, G. M., & Dricker, I. (2014). Characterization of an earthquake sequence triggered by hydraulic fracturing in Harrison County, Ohio. *Seismological Research Letters*, *85*, 1295–1307.

Galloway, E., Hauck, T., Corlett, H., Panǎ, D., & Schultz, R. (2018). Faults and associated karst collapse suggest conduits for fluid flow that influence hydraulic fracturing-induced seismicity. *Proceedings of the National Academy of Sciences of the United States of America*, *115*(43), E10003–E10012.

Ghanizadeh, A., Bhowmik, S., Haeri-Ardakani, O., Sanei, H., & Clarkson, C. (2015a). A comparison of shale permeability coefficients derived using multiple non-steady-state measurement techniques: Examples from the Duvernay Formation, Alberta (Canada). *Fuel*, *140*, 371–387.

Ghanizadeh, A., Clarkson, C., Aquino, S., Ardakani, O. H., & Sanei, H. (2015b). Petrophysical and geomechanical characteristics of Canadian tight oil and liquid-rich gas reservoirs: I. Pore network and permeability characterization. *Fuel*, *153*, 664–681.

Gischig, V., Doetsch, J., Maurer, H., Krietsch, H., Amann, F., Evans, K. F., et al. (2018). On the link between stress field and small-scale hydraulic fracture growth in anisotropic rock derived from microseismicity. *Solid Earth*, *9*(1), 36–61.

Goebel, T. H. W., Weingarten, M., Chen, X., Haffener, J., & Brodsky, E. E. (2017). The 2016 Mw5. 1 Fairview, Oklahoma earthquakes: Evidence for long-range poroelastic triggering at >40 km from fluid disposal wells. *Earth and Planetary Science Letters*, *472*, 50–61.

Green, C. A., Styles, P., & Baptie, B. J. (2012). *Preese Hall shale gas fracturing review and recommendations for induced seismic mitigation*. London: Department of Energy and Climate Change.

Gutenberg, B., & Richter, C. F. (1944). Frequency of earthquakes in California. *Bulletin of the Seismological Society of America*, *34*, 185–188.

Hall, S. A., & J-Kendall, M. (2003). Fracture characterization at Valhall: Application of P-wave amplitude variation with offset and azimuth (AVOA) analysis to a 3D ocean-bottom data set. *Geophysics*, *68*, 1150–1160.

Healy, J. H., Rubey, W. W., Griggs, D. T., & Raleigh, C. B. (1968). The Denver earthquakes. *Science*, *161*(3848), 1301–1310.

Heidbach, O., Rajabi, M., Reiter, K., Ziegler, M., & Team, W. S. M. (2016). *World stress map database release 2016*. Potsdam, Germany: GFZ Data Services.

Hennings, P., Allwardt, P., Paul, P., Zahm, C., Reid, R., Alley, H., et al. (2012). Relationship between fractures, fault zones, stress, and reservoir productivity in the Suban gas field, Sumatra, Indonesia. *AAPG Bulletin*, *96*(4), 753–772.

Holland, A. A. (2013). Earthquakes triggered by hydraulic fracturing in south-central Oklahoma. *Bulletin of the Seismological Society of America*, *103*, 1784–1792.

Hosseini, B., & Eaton, D. W. (2018). *Fluid flow and thermal modeling for tracking induced seismicity near the Graham disposal well, British Columbia, Canada: SEG International exposition and Annual Meeting, 14–19 October*, Anaheim, California, USA.

Huang, L., & Liu, C. Y. (2017). Three types of flower structures in a divergent-Wrench Fault Zone. *Journal of Geophysical Research: Solid Earth*, *122*, 10–478. https://doi.org/10.1002/2017JB014675

Igonin, N. (2020). *Microseismic catalog for ToC2ME dataset (Version 1) [data set]. Zenodo*. http://doi.org/10.5281/zenodo.3900657

Igonin, N., Zecevic, M., & Eaton, D. W. (2018). Bilinear magnitude-frequency distributions and characteristic earthquakes during hydraulic fracturing. *Geophysical Research Letters*, *45*, 12866–12874. https://doi.org/10.1029/2018GL079746

Kao, H., Visser, R., Smith, B., & Venables, S. (2018). Performance assessment of the induced seismicity traffic light protocol for northeastern British Columbia and western Alberta. *The Leading Edge*, *37*, 117–126.

Kendall, J.-M. A., ButcherStork, A. L., Verdon, J. P., Luckett, R., & Baptie, B. J. (2019). How big is a small earthquake? Challenges in determining microseismic magnitudes. *First Break*, *37*, 51–56.

Keranen, K. M., Weingarten, M., Abers, G. A., Bekins, B. A., & Ge, S. (2014). Sharp increase in central Oklahoma seismicity since 2008 induced by massive wastewater injection. *Science*, *345*, 448–451.

Kettlety, T., Verdon, J. P., Hampson, M., & Craddock, L. (2020a). The M$_L$ 2.9 August 2019 earthquake in Lancashire, UK, induced by hydraulic fracturing during Preston New Road PNR-2 operations. *Seismological Research Letters*, *92*(1), 151–169.

Kettlety, T., Verdon, J. P., Werner, M., & Kendall, J.-M. (2020b). Stress transfer from opening hydraulic fractures controls the distribution of induced seismicity. *Journal of Geophysical Research*, *125*, e2019JB018794. https://doi.org/10.1029/2019JB018794

Kettlety, T., Verdon, J. P., Werner, M. J., Kendall, J.-M., & Budge, J. (2019). Investigating the role of elastostatic stress transfer during hydraulic fracturing-induced fault reactivation. *Geophysical Journal International*, *217*, 1200–1216.

Knapp, L., McMillan, J., & Harris, N. (2017). A depositional model for organic-rich Duvernay Formation mudstones. *Sedimentary Geology*, *347*, 160–182.

Kozłowska, M., Brudzinski, M. R., Friberg, P., Skoumal, R. J., Baxter, N. D., & Currie, B. S. (2018). Maturity of nearby faults influences seismic hazard from hydraulic fracturing. *Proceedings of the National Academy of Sciences of the United States of America*, *115*(8), E1720–E1729.

Kwiatek, G., Saarno, T., Ader, T., Bluemle, F., Bohnhoff, M., Chendorain, M., et al (2019). Controlling fluid-induced seismicity during a 6.1-km-deep geothermal stimulation in Finland. *Science Advance 5*, Eaav7224.

Lei, X., Wang, Z., & Su, J. (2019). The December 2018 ML 5.7 and January 2019 ML 5.3 earthquakes in South Sichuan Basin induced by shale gas hydraulic fracturing. *Seismological Research Letters*, *90*, 1099–1110.

Lyster, S., Corlett, H. J., & Berhane, H. (2017). *Hydrocarbon resource potential of the Duverney Formation in Alberta – Update: Alberta energy regulator*. Alberta Geol. Surv. Open File Rep. 2017-02.

Maghsoudi, S., Baro, J., Kent, A., Eaton, D. W., & Davidsen, J. (2018). Interevent triggering in microseismicity induced by hydraulic fracturing. *Bulletin of the Seismological Society of America*, *108*(3A), 1133–1146.

Maxwell, S. C., Jones, M., Parker, R., Leaney, S., Mack, M., Dorvall, D., et al. (2010). Fault activation during hydraulic fracturing. In *72nd EAGE Conference and Exhibition incorporating SPE EUROPEC 2010* (pp. cp-161). The Netherlands: European Association of Geoscientists & Engineers.

Maxwell, S. C., Shemeta, J., Campbell, E., & Quirk, D. (2008). *Microseismic deformation rate monitoring*. (SPE116596). Denver, CO: SPE Annual Technical Conference.

Michael, A. J. (1984). Determination of stress from slip data: Faults and folds. *Journal of Geophysical Research*, *89*, 11517–11526.

Peacock, D. C. P., Nixon, C. W., Rotevatn, A., Sanderson, D. J., & Zuluaga, L. F. (2016). Glossary of fault and other fracture networks. *Journal of Structural Geology*, *92*, 12–29.

Pennington, C., & Chen, X. (2017). Coulomb stress interactions during the MW 5.8 Pawnee sequence. *Seismological Research Letters*, *88*, 1024–1031.

Poulin, A., Weir, R., Eaton, D., Igonin, N., Chen, Y., Lines, L., et al (2019). Focal-time analysis: A new method for stratigraphic depth control of microseismicity and induced seismic events. *Geophysics*, *84*, KS173–KS182.

Questiaux, J.-M., Couples, G., & Ruby, N. (2010). Fractured reservoirs with fracture corridors. *Geophysical Prospecting*, *58*(2), 279–295.

Riazi, N., & Eaton, D. W. (2020). Anatomy of a buried thrust belt activated during hydraulic fracturing. *Tectonophysics*, *795*, 1–9. https://doi.org/10.1016/j.tecto.2020.228640

Rich, J., Bailey, A., Jr, & Klepacki, D. (2019). High- resolution insights into hydraulic fracturing strike-slip seismicity: hypocenter uncertainty, depth of initiation, and genesis mechanisms. In *SEG Technical program Expanded Abstracts*. (pp. 3046–3050). Houston, TX: Society of Exploration Geophysicists.

Rodriguez, G., & Eaton, D. W. (2020). Ground-motion analysis of hydraulic-fracturing induced seismicity at close epicentral distance. *Bulletin of the Seismological Society of America*, *110*(1), 331–344.

Rogers, S. F. (2003). *Critical stress-related permeability in fractured rocks*. Geological Society, London, Special Publications, 209(1), 7–16.

Schoenball, M., Walsh, F. R., Weingarten, M., & Ellsworth, W. L. (2018). How faults wake up: The Guthrie-Langston, Oklahoma earthquakes. *The Leading Edge*, *37*, 100–106.

Schultz, R., Mei, S., Pana, D., Stern, V., Gu, Y. J., Kim, A., & Eaton, D. (2015b). The Cardston earthquake swarm and hydraulic fracturing of the Exshaw Formation (Alberta Bakken play). *Bulletin of the Seismological Society of America*, *105*, 2871–2884.

Schultz, R., Stern, V., Novakovic, M., Atkinson, G., & Gu, Y. J. (2015a). Hydraulic fracturing and the Crooked Lake sequences: Insights gleaned from regional seismic networks. *Geophysical Research Letters*, *42*, 2750–2758. https://doi.org/10.1002/2015GL063455

Schultz, R., & Wang, R. (2020). Newly emerging cases of hydraulic fracturing induced seismicity in the Duvernay East Shale Basin. *Tectonophysics*, *779*, 228393.

Schultz, R., Wang, R., Gu, Y. J., Haug, K., & Atkinson, G. (2017). A seismological overview of the induced earthquakes in the Duvernay play near Fox Creek, Alberta. *Journal of Geophysical Research: Solid Earth*, *122*, 492–505. https://doi.org/10.1002/2016JB013570

Segall, P., & Lu, S. (2015). Injection-induced seismicity: Poroelastic and earthquake nucleation effects. *Journal of Geophysical Research: Solid Earth*, *120*, 5082–5103. https://doi.org/10.1002/2015JB012060

Shapiro, S., & Dinske, C. (2009). Fluid-injection seismicity: Pressure diffusion and hydraulic fracturing. *Geophysical Prospecting*, *57*(2), 301–310.

Shipman, T., MacDonald, R., & Byrnes, T. (2018). Experiences and learnings from induced seismicity regulation in Alberta. *Interpretation*, *6*(2), SE15–SE21.

Skoumal, R. J., Brudzinski, M. R., & Currie, B. S. (2015). Induced earth-quakes during hydraulic fracturing in Poland Township, Ohio. *Bulletin of the Seismological Society of America*, *105*, 189–197.

Skoumal, R. J., Kaven, J. O., & Walter, J. I. (2019). Characterizing seismogenic fault structures in oklahoma using a relocated template-matched catalog. *Seismological Research Letters*, *90*(4), 1535–1543.

Soltanzadeh, M., Davies, G., Fox, A., Hume, D., & Rahim, N. (2015). *Application of mechanical and mineralogical rock properties to identify fracture fabrics in the Devonian Duvernay formation in Alberta: Unconventional Resources Technology Conference, URTeC 2178289*.

Stein, R. S., King, G. C. P., & Lin, J. (1992). Change in failure stress on the southern San Andreas fault system caused by the 1992 magnitude = 7.4 Landers earthquake. *Science*, *258*, 1328–1332.

Talwani, P., & Acree, S. (1984). Pore pressure diffusion and the mechanism of reservoir-induced seismicity. *Pure and Applied Geophysics*, *122*, 947–965.

Teanby, N. A., Kendall, J.-M., & van der Baan, M. (2004). Automation of shear-wave splitting measurements using cluster analysis. *Bulletin of the Seismological Society of America*, *94*, 453–463.

Townend, J., & Zoback, M. D. (2004). Regional tectonic stress near the San Andreas fault in central and southern California. *Geophysical Research Letters*, *31*, L15S11. https://doi.org/10.1029/2003GL018918

Urbancic, T. I., Shumila, V., Rutledge, J. T., & Zinno, R. J.. (1999). *Determining hydraulic fracture behavior using microseismicity*. San Francisco, CA: American Rock Mechanics Association.

van der Elst, N. J., Savage, H. M., Keranen, K. M., & Abers, G. A. (2013). Enhanced remote earthquake triggering at fluid-injection sites in the midwestern United States. *Science*, *341*, 164–167.

Verdon, J. P., & Bommer, J. (2020). Green, yellow, red, or out of the blue? An assessment of Traffic Light Schemes to mitigate the impact of hydraulic fracturing-induced seismicity. *Journal of Seismology*, *24*(5), 1–26. https://doi.org/10.1007/s10950-020-09966-9

Verdon, J. P., & Budge, J. (2018). *Examining the capability of statistical models to mitigate induced seismicity during hydraulic fracturing of shale gas reservoirs* (Vol. 108, pp. 690–7010). Bulletin of the Seismological Society of America.

Verdon, J. P., Kendall, J.-M., Hicks, S. P., & Hill, P. (2017). Using beamforming to maximize the detection capability of small, sparse seismometer arrays deployed to monitor oil field activities. *Geophysical Prospecting*, *65*, 1582–1596.

Verdon, J. P., Stork, A. L., Bissell, R. C., Bond, C. E., & Werner, M. J. (2015). Simulation of seismic events induced by CO2 injection at In Salah, Algeria. *Earth and Planetary Science Letters*, *426*, 118–129.

Verdon, J. P., Wuestefeld, A., Rutledge, J. T., Main, I. G., & Kendall, J.-M. (2013). Correlation between spatial and magnitude distributions of microearthquakes during hydraulic fracture stimulation. *75th EAGE Conference, London, Expanded Abstracts Th-01-12*.

Viegas, G., Urbancic, T., & Chittenden, H. (2018). Influence of geological setting on stress released by hydraulic fracture-induced earthquakes. *First Break*, *36*, 77–81.

Wang, R., Gu, Y. J., Schultz, R., & Chen, Y. (2018). Faults and non-double-couple components for induced earthquakes. *Geophysical Research Letters*, *45*, 8966–8975. https://doi.org/10.1029/2018GL079027

Wang, R., Gu, Y. J., Schultz, R., Kim, A., & Atkinson, G. (2016). Source analysis of a potential hydraulic-fracturing-induced earthquake near Fox Creek, Alberta. *Geophysical Research Letters*, *43*, 564–573. https://doi.org/10.1002/2015GL066917

Wang, R., Lorenzo Martín, F., & Roth, F. (2006). PSGRN/PSCMP—A new code for calculating co- and post-seismic deformation, geoid and gravity changes based on the viscoelastic-gravitational dislocation theory. *Computers & Geosciences*, *32*(4), 527–541.

Weir, R., Eaton, D., Lines, L., Lawton, D., & Ekpo, E. (2017). Inversion and interpretation of seismic-derived rock properties in the Duvernay play. *Interpretation*, *6*(2), SE1–SE14.

Westaway, R. (2017). Integrating induced seismicity with rock mechanics: A conceptual model for the 2011 Preese Hall fracture development and induced seismicity. In E. H. Rutter, J. Mecklenburgh, & K. G. Taylor (Eds.), *Properties of mudrocks* (Vol. 454, pp. 327–359). London: Geological Society of London Special Publications.

Westwood, R. F., Toon, S. M., Styles, P., & Cassidy, N. J. (2017). Horizontal respect distance for hydraulic fracturing in the vicinity of existing faults in deep geological reservoirs: A review and modeling study. *Geomechanics and Geophysics for Geo-Energy and Geo-Resources*, *3*, 379–391.

Wilson, M. P., Worrall, F., Davies, R. J., & Almond, S. (2018). Fracking: How far from faults?. *Geomechanics, Geophysics and Geophysics for Geo-Energy and Geo-Resources*, *4*, 193–199.

Zhang, H., Eaton, D. W., Li, G., Liu, Y., & Harrington, R. M. (2016). Discriminating induced seismicity from natural earthquakes using moment tensors and source spectra. *Journal of Geophysical Research: Solid Earth*, *121*, 972–993. https://doi.org/10.1002/2015JB012603

Zhang, H., Eaton, D. W., Rodriguez, G., & Jia, S. Q. (2019). Source-mechanism analysis and stress inversion for hydraulic-fracturing-induced event sequences near Fox Creek, Alberta. *Bulletin of the Seismological Society of America*, *109*(2), 636–651. https://doi.org/10.1785/0120180275

Zoback, M., & Kohli, A. (2019). *Unconventional reservoir geomechanics: Shale gas, tight oil, and induced seismicity*. Cambridge, UK: Cambridge University Press.